JGR Solid Earth

RESEARCH ARTICLE
10.1029/2019JB018117

Sharp Lateral Moho Variations Across the SE Tibetan Margin and Their Implications for Plateau Growth

Mijian Xu[1], Zhouchuan Huang[1], Liangshu Wang[1], Mingjie Xu[1], Yueqiao Zhang[1], Ning Mi[1], Dayong Yu[1], and Xiaohui Yuan[2]

[1]State Key Laboratory for Mineral Deposits Research, School of Earth Sciences and Engineering, Nanjing University, Nanjing, China, [2]GeoForschungsZentrum Potsdam, Potsdam, Germany

Key Points:
- We mapped the Moho depths under SE Tibet revealed by receiver function analysis
- Large Moho depth gradients are found beneath the boundary faults along the SE Tibetan margin
- The evolution of SE Tibet involved crustal thickening during block extrusion and subsequent surface topography smoothing by gravity collapse

Supporting Information:
- Supporting Information S1
- Data Set S1
- Data Set S2
- Data Set S3

Correspondence to:
M. Xu and Z. Huang,
gomijianxu@gmail.com;
huangz@nju.edu.cn

Citation:
Xu, M., Huang, Z., Wang, L., Xu, M., Zhang, Y., Mi, N., et al. (2020). Sharp lateral Moho variations across the SE Tibetan margin and their implications for plateau growth. *Journal of Geophysical Research: Solid Earth*, *125*, e2019JB018117. https://doi.org/10.1029/2019JB018117

Received 30 MAY 2019
Accepted 15 APR 2020
Accepted article online 20 APR 2020

Abstract The tectonic uplift of the Tibetan Plateau is a focus in the geosciences. Middle-lower crustal flow is a popular model to interpret the geodynamic mechanism on the margin of the Tibetan Plateau. The model predicts different surface and Moho topographies across the plateau boundary due to the different strengths of the surrounding blocks, that is, sharp boundaries on the eastern plateau boundary and gentle variations in the southeastern plateau boundary. Here, we employ receiver function and common conversion point stacking analysis with the seismic waveforms recorded by the dense ChinArray and other local seismic stations to accurately define the Moho topography in southeastern (SE) Tibet. We find that the Moho under the Tibetan Plateau is much deeper than that under the surrounding Yangtze Craton and Indochina block; abrupt Moho changes are found across the southeastern plateau margin, similar to that under the eastern plateau margin. We interpret these sharp Moho variations across the plateau margin to have developed when the Tibetan Plateau was extruded southeastward in the late Miocene. Subsequent gravity collapse resulted in crustal extension and gentle topographic variation, while the sharp Moho slope was preserved.

1. Introduction

In contrast with sharp lateral variations in surface morphology and Moho depth across the Longmenshan fault zone on the eastern Tibetan margin, the southeastern (SE) Tibetan margin displays a relatively gentle variation in topography and diffuse pattern of surface deformation (e.g., Qian et al., 2018; Z. Zhang et al., 2009) (Figure 1a). Models proposed to account for the plateau's eastward growth include block extrusion guided by large-scale strike-slip faults (Molnar & Tapponnier, 1975; Tapponnier et al., 1982, 2001), continuous crustal shortening and thickening (England & Houseman, 1986; Yang & Liu, 2013), and lower crustal channel flow (Clark & Royden, 2000; Royden et al., 2008).

Specifically, the model of lower crustal flow explains the crustal thickening in the Tibetan margin well and has been supported by geophysical results in recent years, including high-conductivity anomalies (e.g., Bai et al., 2010), low-velocity anomalies (e.g., Bao et al., 2015; M. Chen et al., 2014; Fu et al., 2017; Z. Huang et al., 2018; Liu et al., 2014; W. Wang et al., 2014; Wei et al., 2013; Yao et al., 2008, 2010), and positive radial anisotropies ($V_{SH} > V_{SV}$) (H. Huang et al., 2010; Xie et al., 2017) and by GPS measurements (Shen et al., 2005). Previous receiver function studies have shown a gentle variation in the Moho topography from the Tibetan Plateau to the Yangtze Craton (e.g., Sun et al., 2012; W. Wang et al., 2017; X. Xu et al., 2013), consistent with the Moho variation predicted by the lower crustal flow model.

The SE Tibetan margin involves part of the Songpan-Ganze terrane, the Yangtze Craton, and the Indochina Block (Figure 1b). Both strike-slip faults and thrust faults have been documented along this margin, for example, the Lijiang-Xiaojinhe fault (LXF), Muli thrust zone (MT), Jinhe-Qinghe thrust zones (JQT), and Red River fault (RRF). The Zemuhe fault (ZMHF) and Xiaojiang fault (XJF) divide the Yangtze Craton into subblocks such as the Dianzhong subblock. The surface strain field inverted from GPS observations (Figure 1a) indicates strong deformations only along the boundary faults (Kreemer et al., 2014). Previous surface wave inversions, while revealing widespread low-velocity zones across the whole lower crust beneath the high plateau, have found only low-velocity belts bounded by major faults in SE Tibet (e.g., Bao et al., 2015; M. Chen et al., 2014; W. Wang et al., 2014; Yao et al., 2008). These results indicate that in SE Tibet, the lower crust is affected by major faults.

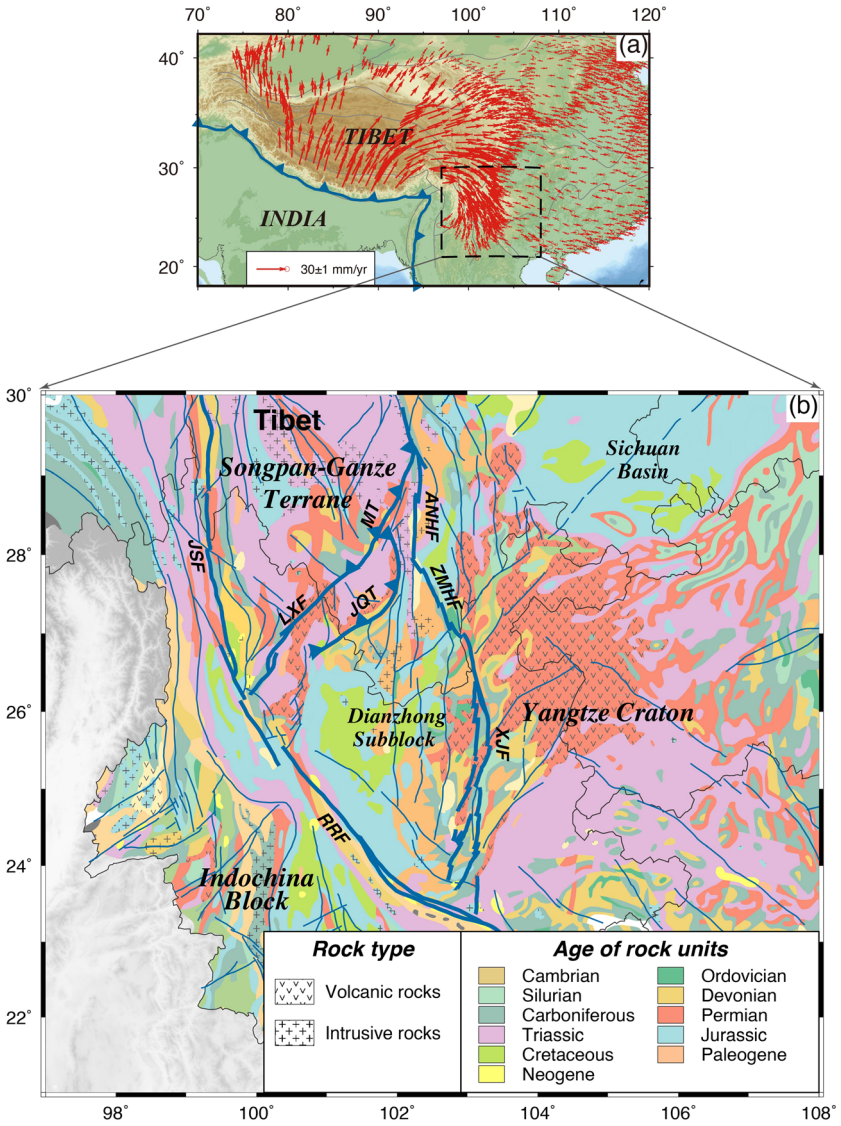

Figure 1. (a) Tectonic background of the Tibetan Plateau and adjacent regions. The solid and gray curves denote major boundaries between different blocks. The blue curve with triangles denotes the Himalaya fold belt. The red arrows represent crustal motions relative to the stable Eurasian plate from GPS measurements (Zhao et al., 2015). The dashed box shows our study region. (b) Geological map of SE Tibet (Central Energy Resources Team, 2016). The blue lines represent faults; the thick blue lines show important boundary faults. The abbreviations are ANHF: Anninghe fault; JSF: Jinshajiang fault; LXF: Lijiang-Xiaojinhe fault; MT: Muli thrust zone; JQT: Jinghe-Qinghe thrust zone; RRF: Red River fault; XJF: Xiaojiang fault; ZMHF: Zemuhe fault.

It remains unclear how deep these faults extend downward and whether they cut through the Moho. The gentle Moho topography revealed in previous studies does not support the notable influence of the faults on the Moho. However, these studies determined the Moho depth with $H - \kappa$ stacking analysis (e.g., W. Wang et al., 2017), which yields an average value under each station. These measurements may deviate from the actual structure when a dipping Moho exists, such as in SE Tibet. Thus, the Moho topography in SE Tibet needs to be reanalyzed in detail. Detailed Moho topography may provide important information on crustal evolution. In contrast to the crustal flow model (Royden et al., 2008), deep boundary faults tend to produce steeply sloping Moho discontinuities or even Moho steps.

In this study, we employ *P* wave receiver functions (PRFs) (Langston, 1979; Ligorría & Ammon, 1999) with data mainly collected by the dense stations of the ChinArray (Phases 0 and 1; part of the data used by W. Wang et al., 2017) (35 km average lateral interval) (Figure 2a) and use the common conversion point

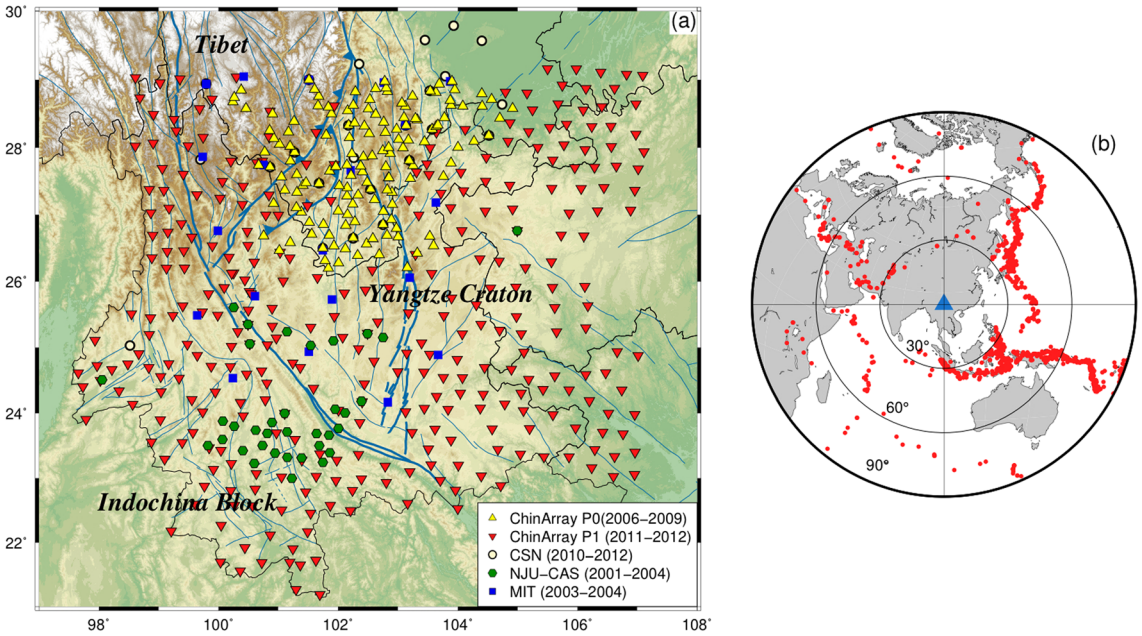

Figure 2. (a) Stations used in this study. Yellow triangles represent temporary stations of the ChinArray project phase 0; inverted red triangles represent the temporary stations of the ChinArray project phase 1; yellow circles represent permanent stations of the Chinese Seismic Network (CSN); green circles represent the portable stations deployed by Nanjing University and the Chinese Academy of Sciences (NJU-CAS); blue squares represent temporary stations deployed by the Massachusetts Institute of Technology (MIT). Thick and thin blue lines denote major tectonic boundaries and active faults, respectively. (b) Earthquakes (red dots) used for receiver function analysis in this study. The blue triangle represents the center of the study region.

(CCP) stacking method (Dueker & Sheehan, 1997) to estimate the Moho depths. The high-resolution Moho topographic map reveals a sharp Moho gradient zone across the SE Tibetan margin, which provides important clues to understand the tectonic evolution of SE Tibet.

2. Data and Method

We used the records of 548 three-component broadband stations from five different networks in SE Tibet (Figure 2a): (1) 145 temporary stations of ChinArray Phase 0 (October 2006 to July 2009; yellow triangles in Figure 2a), (2) 325 temporary stations of ChinArray Phase 1 (October 2011 to August 2012; inverted red triangles in Figure 2a), (3) 24 permanent stations of the Chinese Seismic Network (January 2010 to June 2012; yellow circles in Figure 2a), (4) 34 portable stations deployed by Nanjing University and the Chinese Academy of Sciences (July 2001 to August 2004; green hexagons in Figure 2a), and (5) 20 portable stations operated by the Massachusetts Institute of Technology (October 2003 to September 2004; blue squares in Figure 2a). We selected teleseismic events with magnitudes greater than 5.5 and epicentral distances of 30–90°. The back azimuthal coverage of the events was relatively good; however, more events occurred in the circum-Pacific and Indonesian subduction zones (Figure 2b) than in other places.

First, we removed the mean shift and linear trend in the waveforms and filtered them with a fourth-order Butterworth filter in the band of 0.05–2 Hz. Then, we rotated the horizontal components into radial and transverse components. We calculated the signal-to-noise ratios (SNRs) by

$$SNR = 10ln\left(\frac{A_s}{A_N}\right)^2 \quad (1)$$

where A_N and A_S are root-mean-squares of the waveform in 100 s time windows before and after the theoretical P arrival time calculated by the Taup toolkit (Crotwell et al., 1999), respectively. We cut the records with SNR above 7.0 from 10 s before to 120 s after theoretical P arrival times and then calculated the PRFs by a time domain iterative deconvolution (Ligorría & Ammon, 1999) with a maximum iteration of 400 or a misfit reduction of less than 0.001 between the last two iterations. Finally, we manually

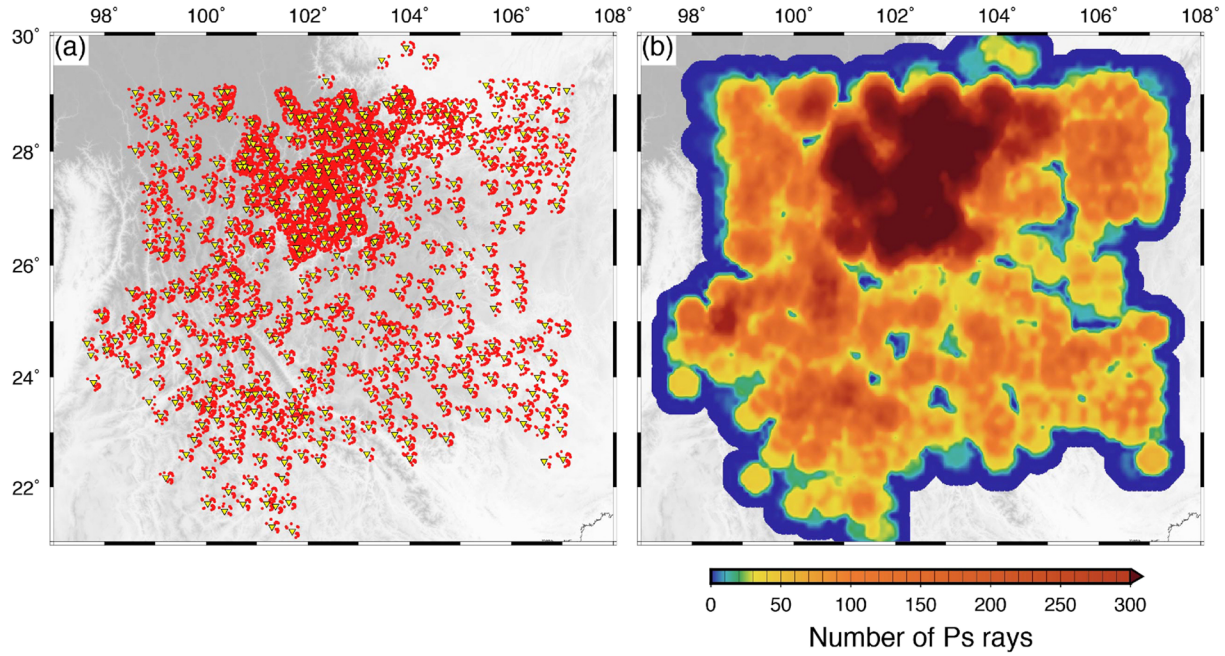

Figure 3. (a) Ps piercing points at a depth of 45 km. The inverted yellow triangles represent stations. The red dots denote Ps piercing points. (b) Number of piercing points within each bin. The bin radius is set by Fresnel zones.

checked the PRFs and removed those containing weak *P* phases, unexpectedly large amplitudes, or low-frequency oscillations. In the end, we obtained a total of 48,984 high-quality PRFs.

We stacked the PRFs with the CCP stacking method (Dueker & Sheehan, 1997). The differential time between *Ps* and direct *P* depends on the length of the ray path from the piercing point to the station and the velocity structure (i.e., V_P and V_S). The ray path length L_{Ps} from a certain depth (0–100 km) is calculated by (Eagar et al., 2010; M. Xu et al., 2018):

$$L_{Ps} = \sum_i^N \left(\frac{1}{\sqrt{\left(\frac{R(i)}{pV_S(i)}\right)^2 - 1}} \right) \frac{\Delta r}{R(i)} \tag{2}$$

where $R(i)$ is the Earth's radius from the i*th* layer (in km), N is the number of layers, r is the depth interval, p is the ray parameter of the direct *P* wave, and $V_S(i)$ is the *S* wave velocity at the i*th* layer in the IASP91 model (Model I) (Kennett & Engdahl, 1991). We accumulate L_{Ps} from 0 to 100 km with a depth interval of 1 km (i.e., $i = 0$, $N = 100$, $r = 1$). For each depth, the *Ps*-*P* differential time T_{Ps} is calculated by (Eagar et al., 2010; M. Xu et al., 2018):

$$T_{Ps} = \sum_i^N \left(\sqrt{\left(\frac{R(i)}{V_S(i)}\right)^2 - p^2} - \sqrt{\left(\frac{R(i)}{V_P(i)}\right)^2 - p^2} \right) \frac{\Delta r}{R(i)} \tag{3}$$

where $V_P(i)$ is the *P* wave velocity at the i*th* layer in the IASP91 model (Model I). The amplitudes are linearly interpolated by T_{Ps} at each depth.

To investigate the influence of crustal velocities on the time-to-depth conversion, we applied two different 3-D local *P* and *S* wave velocity models to calculate L_{Ps} and T_{Ps} (Models II and III). In Model II, the *S* wave velocity model is derived from Bao et al. (2015) by joint inversion of Rayleigh wave dispersion and PRFs. The *P* wave velocities are estimated using crustal average V_P/V_S ratios determined by the $H - \kappa$ stacking method (W. Wang et al., 2017). In Model III, while using the same V_S model, we use a local *P* wave velocity model

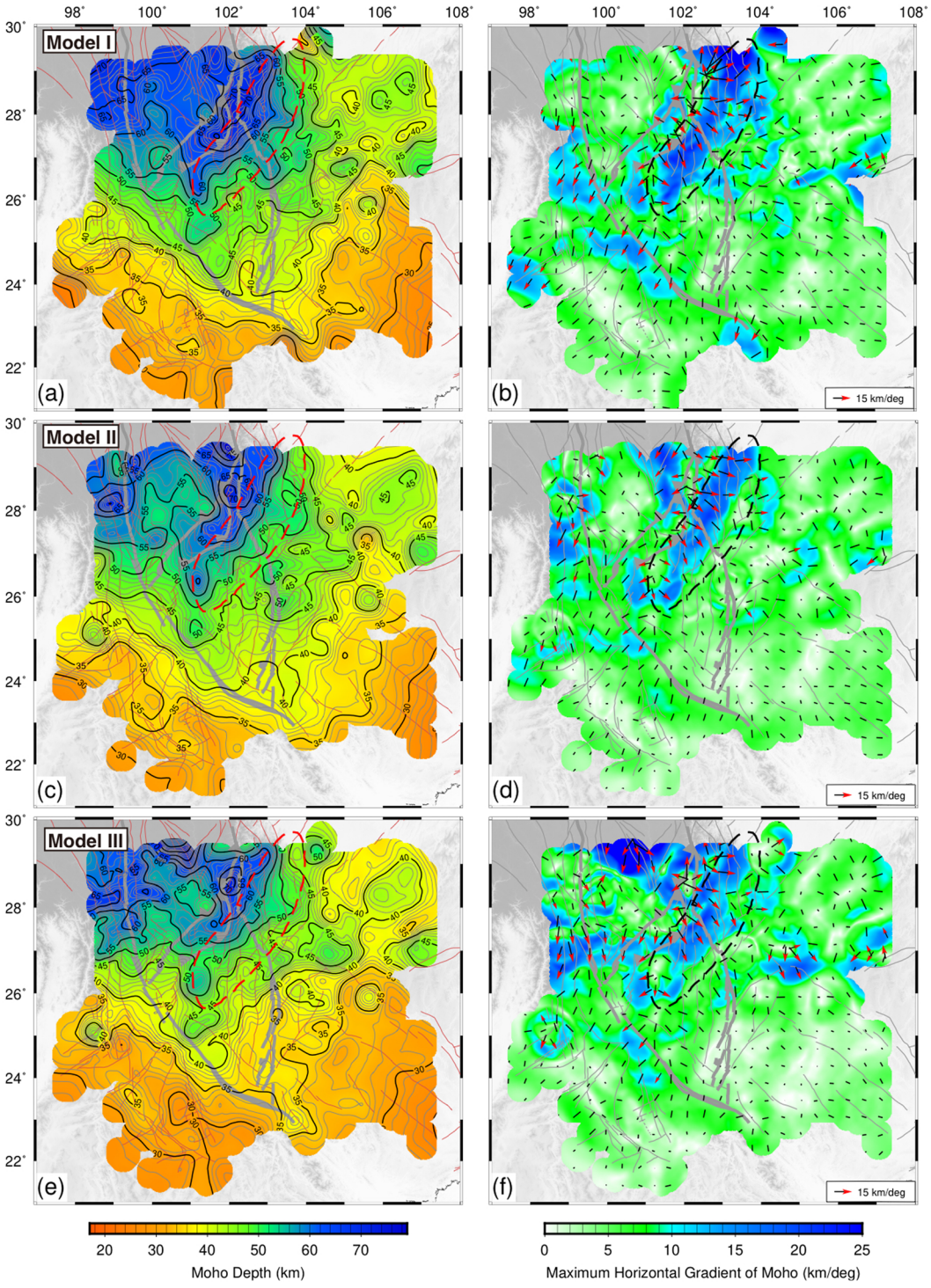

Figure 4. (a, c, and e) Maps of Moho depth obtained by searching positive peaks of P_ms in the CCP stacking images (see the text for details). Red solid lines represent faults. Thick gray lines represent major faults. Red dashed curves denote the observed Moho gradient zones. (b, d, and f) Maximum horizontal gradients of the Moho depth. Thin and thick gray lines represent faults and major faults, respectively. Short bars denote the directions of maximum gradients at every grid; red arrows show the grids with corresponding gradients >10 km/degree. Black dashed curves denote the observed Moho gradient zones.

determined by travel time tomography (Z. Huang et al., 2018). We construct a 1-D velocity model beneath each station from the 3-D models and calculate L_{Ps} and T_{Ps} by equations 2 and 3, respectively.

Because the receiver function yields more reasonable values of crustal V_P/V_S ratios in Model II (W. Wang et al., 2017), we calculate CCP stacks along 13 profiles using Model II (Figures S1–S3 in the supporting information) to map the lateral Moho depth variations. We move rectangular bins along the profiles at a step of 5 km for the stacking, where the width perpendicular to the profiles is 100 km, and the lengths parallel to the profiles are determined by the Fresnel zone diameter. Given the good coverage of the P_ms rays (Figure 3), we also determine the Moho depth by picking the P_ms phases on the 3-D CCP stacked PRFs instead of using the traditional $H-\kappa$ stacking method. We set up lateral nodes with intervals of 0.1° and stack PRFs whose L_{Ps} is less than the radius of a circular bin (the radius determined by the Fresnel zone) centered on each node from depths of 0–100 km. We automatically search for maximum positive P_ms peaks around the Moho depth (±15 km) determined by Bao et al. (2015). The numbers of PRFs are greater than 40 at most nodes (Figure 3b). To avoid abnormal values of Moho depth at individual nodes, we virtually check every node. We refer to the Moho depth in profiles (Figures S1–S3) to select the most reasonable peaks in nodes, especially where the Moho changes abruptly. We select the peak with the largest amplitude in the same node. However, the node is rejected if it has two or more peaks with comparable amplitudes. Finally, we obtain the Moho depths at 4,748 nodes in SE Tibet (Figure 4).

3. Results

The Moho topography derived from Model I shows complex crustal structures in SE Tibet (Figure 4a and Data Set S1). The Moho depth ranges from 25 to 74 km. In general, the Moho depth increases from 55–65 km in the Songpan-Ganze terrane to 65–74 km under the JQT and decreases to ~40–50 km under the Dianzhong subblock and ~30–40 km beneath the Indochina block and the Yangtze Craton. The first-order pattern of the Moho variations (i.e., the Moho is deeper under the Tibetan Plateau and shallower southeastward under the Yangtze and Indochina blocks) is consistent with results obtained by previous seismic studies (e.g., Bao et al., 2015; Sun et al., 2012; W. Wang et al., 2017; L. Xu et al., 2007; X. Xu et al., 2013).

Lateral heterogeneities in crustal thickness and velocities have been observed in SE Tibet by previous seismic studies (e.g., Bao et al., 2015; Z. Huang et al., 2018; Y. Sun et al., 2012; W. Wang et al., 2017; Yao et al., 2008). Removing the effect of the structural heterogeneities, Models II (Figure 4c and Data Set S2) and III (Figure 4e and Data Set S3) result in lateral Moho variations similar to those in Model I. The first-order pattern, for example, decreasing Moho depth southeastward with a local depression (~70 km) under the JQT, is consistent across all three models. However, some details are different. For example, due to the thickened crust and crustal low-velocity zones in the Songpan-Ganze terrane, the Moho is estimated to be 55–65 km by Model I, 53–60 km by Model II, and 58–68 km by Model III.

The Moho topography is complex near major boundary faults such as the MT and JQT (Figures 4a, 4c, and 4e). An apparent steeply sloping Moho is found adjacent to the JQT (Figures 5a and 5b), indicating the potential influence of the major faults on the Moho discontinuity. In particular, in Figure 5b, the Moho is depressed from 55 to 62 km under the MT and then shallows to 48 km southeastward to the ZMHF. Previous studies have also found a deeper Moho beneath the Songpan-Ganze terrane than under the Dianzhong subblock (Bao et al., 2015; Sun et al., 2012; W. Wang et al., 2017; X. Xu et al., 2013), although they show a gently sloping Moho in general.

To highlight the spatial distribution of the abrupt lateral Moho variations, we calculate the maximum horizontal gradient of the Moho (MHGM) as follows: (1) We apply an equally weighted spatial filter to the Moho depths in Figures 4a, 4c, and 4e with a filter radius of 50 km; (2) we calculate the first-order difference in the Moho depth at each node along both the longitudinal and latitudinal directions; and (3) we obtain the MHGM from vector summations of the longitudinal and latitudinal gradients.

Figures 4b, 4d, and 4f show the distribution of the MHGM in SE Tibet. A gradient zone with large lateral gradients is visible in all three models. Taking Model II as an example (Figure 4d), the gradient zone is parallel to the MT-JQT. The Moho becomes shallower from more than 70 to ~50 km southeastward, with a MHGM of 12–30 km/degree. The MHGM directions are perpendicular to the MT and JQT but consistent with the directions of crustal motion and maximum horizontal stress (e.g., Z. Xu et al., 2016; Zhao

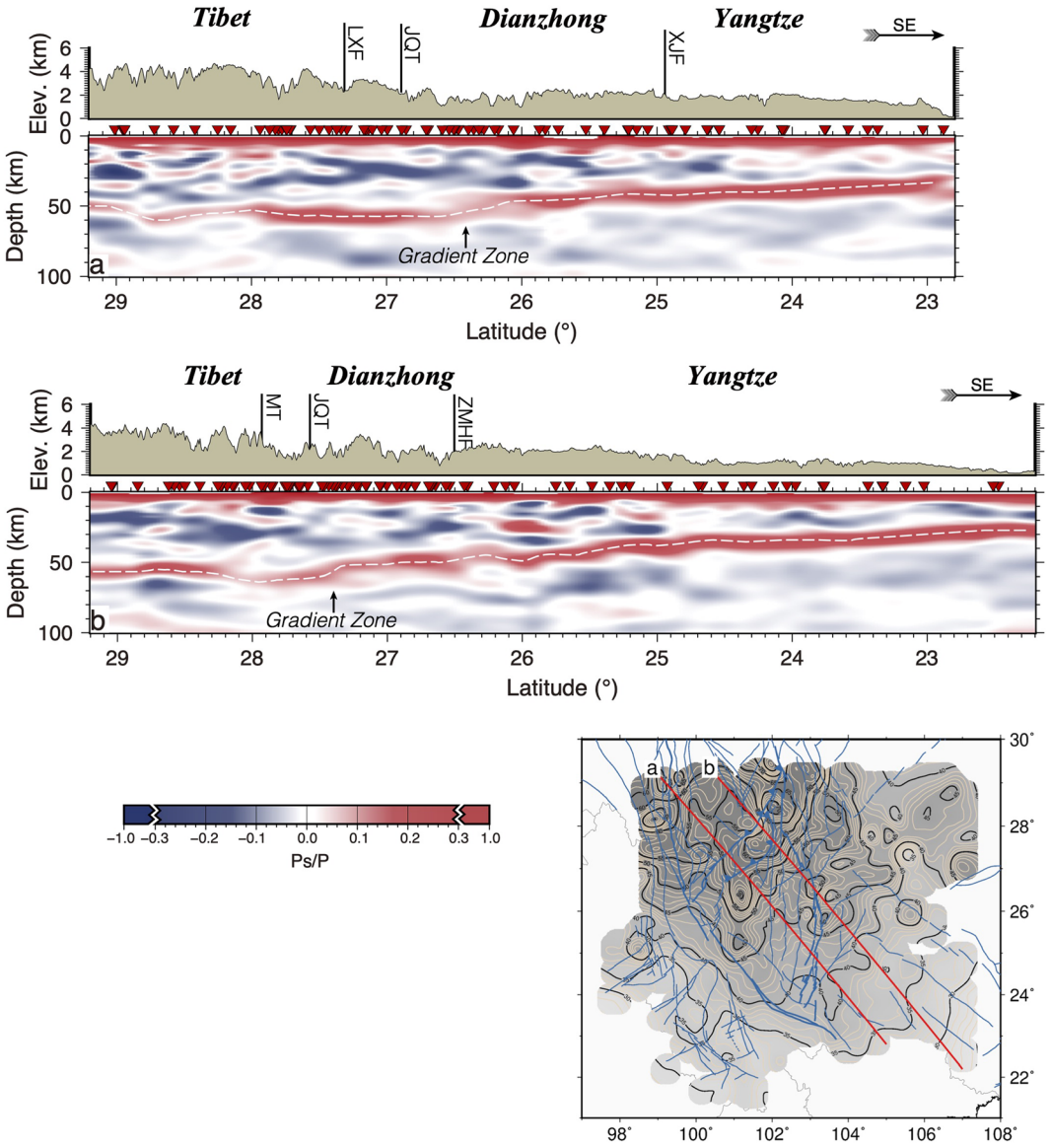

Figure 5. Cross sections of CCP stacking images with topography along two profiles shown in the bottom right inset. The red colors indicate positive phases (increased velocity downward); the blue colors indicate negative phases (decreased velocity downward).

et al., 2015). This observation indicates that crustal deformation produces a steeply sloping Moho in SE Tibet. Note that Model III uses V_P and V_S values from completely different inversions so that the V_P/V_S ratios span a wide range. However, the first-order pattern of the Moho topography is similar to that for Model II. The large gradient zone along the SE plateau margin is also notable, indicating a robust feature that is little affected by the velocity models.

4. Discussion

4.1. The Moho Gradient Zone

In this study, the Moho depth varies from 24 to 75 km under SE Tibet. A sharp Moho gradient zone is observed southeast of the MT-JQT fault zones. Previous studies have revealed a gentle Moho topography across these boundary zones (e.g., Bao et al., 2015; Sun et al., 2012; W. Wang et al., 2017; X. Xu et al., 2013). In particular, W. Wang et al. (2017) estimated the Moho depth in SE Tibet using similar data sets (Figure S4a)

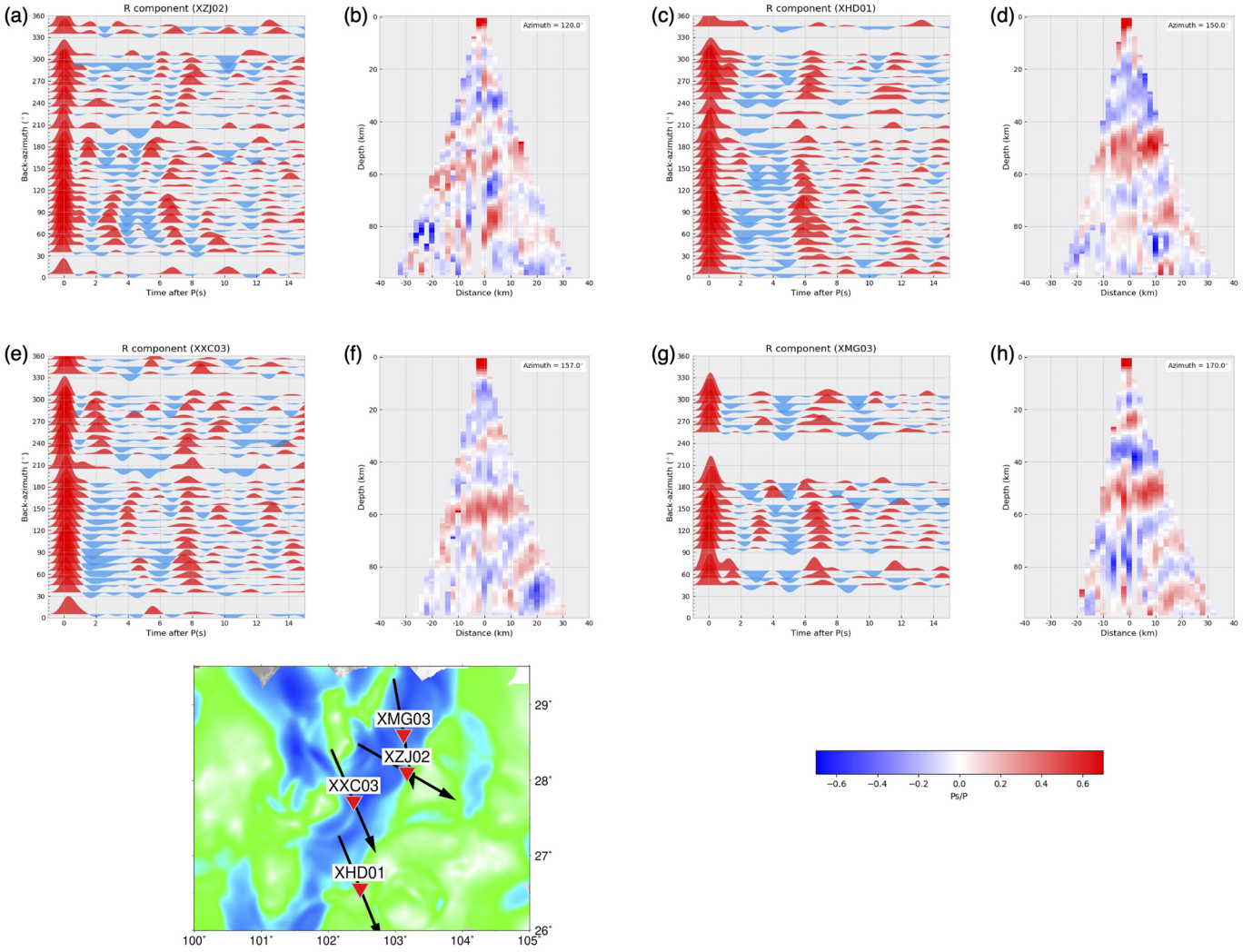

Figure 6. (a, c, e, and g) Stacked PRFs at stations XZJ02, XHD01, XXC03, and XMG03, respectively, sorted by back azimuth. The locations of the stations are shown as inverted red triangles in the bottom-right inset. (b, d, f, and h) CCP stacked PRFs of these stations along the back azimuths of 120°,150°, 157°, and 170° (black arrows), respectively. Red colors denote positive phases; blue colors denote negative phases.

by the $H-\kappa$ stacking method (Zhu & Kanamori, 2000). The map of Moho depth is generally consistent with our observations. However, it does not show a sharp Moho gradient zone. We calculated the MHGM from the results of W. Wang et al. (2017) (Figure S4b). No obvious sharp gradient in the lateral Moho variations is found near the MT-JQT. The present study yields a deeper Moho to the northwest of the MT-JQT than that of W. Wang et al. (2017) (Figure S5). We argue that the $H-\kappa$ stacking method used by W. Wang et al. (2017) does not consider the effects of the dipping interface on PRFs with different back azimuths. When the dip angle of the Moho under a station is large, the $H-\kappa$ stacking method provides an average value of the Moho depth, which would be smaller than the real Moho depth (P. Wang et al., 2010).

To illustrate this effect, we performed further synthetic tests. We first assumed a simple model with a flat Moho at 52 km depth and a crustal V_P/V_S of 1.73 and then generated synthetic waveforms with the RAYSUM package (Frederiksen & Bostock, 2000). With the same weights (0.6, 0.3, and 0.1 for *Ps*, *PpPs*, and *PsPs+PpSs*) as in W. Wang et al. (2017), the $H-\kappa$ stacking method estimates the Moho depth correctly (Figure S6). However, if the Moho has a dip angle of 20° (the azimuth of the strike is 270°), the estimation by the $H-\kappa$ stacking method yields a shallower Moho (45.7 km) (Figure S7). Indeed, stations along the gradient zone show that the P_ms peaks exhibit a periodic change with the back azimuth. For example, we sorted the PRFs at stations XZJ02, XXC03, XHD01, and XMG03 by back azimuth and stacked them in each 10° bin

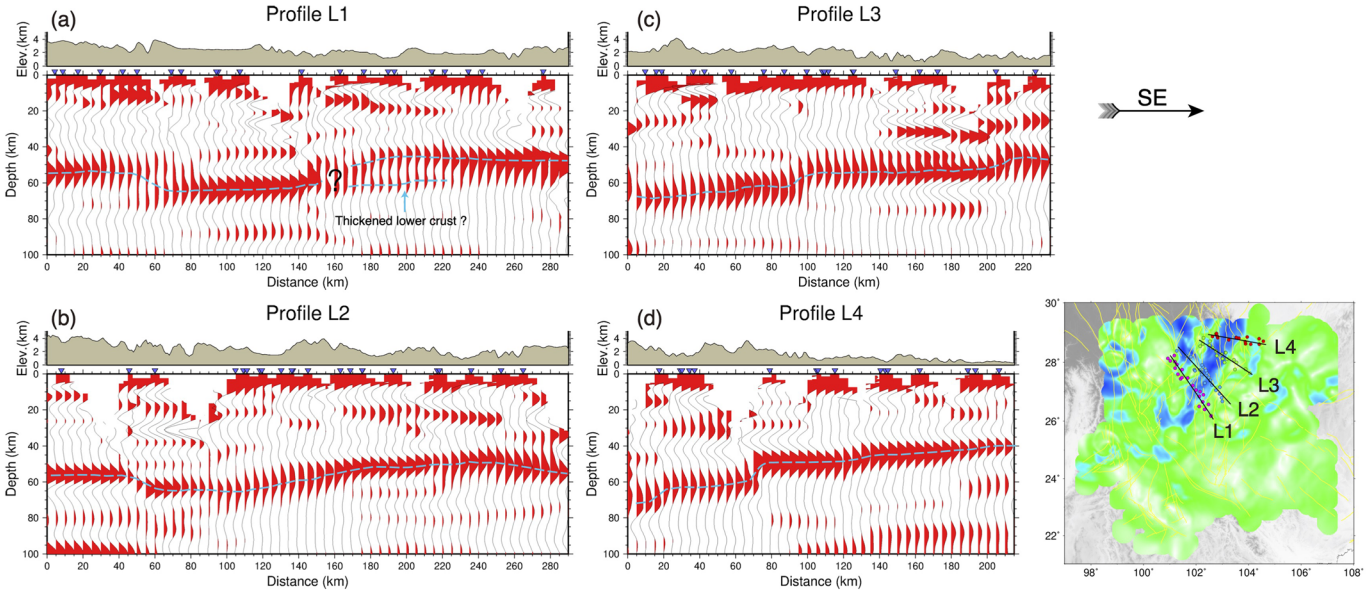

Figure 7. (a–d) Stacked PRFs along four profiles shown in the right inset. Red colors denote positive phases. Dashed blue lines represent the Moho variations. Colored circles along the profiles in the right inset denote the stations used to generate the stacked PRFs in (a)–(d).

to characterize the variations in P_ms peaks (Figures 6a, 6c, 6e, and 6g). The *Ps-P* time differences first decrease and then increase with back azimuths from 0° to 360°. We stacked the amplitudes of PRFs after time-to-depth conversions along the back azimuth so that the minimum *Ps-P* time differences appeared. The oblique Moho is clearly observed at these stations (Figures 6b, 6d, 6f, and 6h). However, due to complex crustal structures such as crustal heterogeneities and anisotropies in the study region, azimuthal variations are not notable at other stations. The CCP stacking method considers the azimuthal variations in the PRFs at different stations. Dense station coverage allows the CCP stacking method to reduce the lateral heterogeneities and the effect of anisotropy map a more accurate Moho depth to the first order.

To map the Moho depth more accurately, we calculated the CCP stacking images along four profiles (the width of the profile is 40 km) across the gradient zone. Profiles L1–L4 indicate that the Moho varies by ~10–18 km across the MT-JQT (Figure 7). These sections imply different changes in the Moho discontinuities across the major boundary faults in SE Tibet. To illustrate the lateral Moho variations in different profiles, we tested the effects of different Moho topographies on CCP stacking (Figures 8 and 9). Here, we used the 2-D spectral element method (Tromp et al., 2008) to calculate synthetic seismograms with incident plane waves of different ray parameters recorded by 20 stations at equal intervals (10 km) along the profile. We deconvolved the R component by the Z component to obtain the synthetic PRFs and stacked the PRFs with the CCP stacking method.

Along Profile L1, double phases appear from 160 to 180 km in the lower crust, adjacent to the Moho step. Considering the presence of the upper crustal *Ps* phases above the double phase, we selected some stations to verify whether these phases at ~60 km depth are caused by multiple phases of an upper crustal layer. Figure S8 shows the stacked PRFs sorted by ray parameters. The synthetic arrivals of the upper crustal *Ps* phases and their multiple phases were calculated. We find that the calculated multiple phases do not correlate with the observed phases as a whole. Therefore, we believe that the double phases are derived by interfaces in the lower crust rather than multiple crustal phases. We set a crustal model with a transition zone (15 km thick) in the lower crust and a dipping Moho (Figure 8a). Double phases similar to those in Profile L1 appear in the synthetic CCP stacking image (Figure 8b). This model is consistent with the thickened lower crust measured by *S* wave velocity changing from 4 to 4.5 km/s in this region (Liu et al., 2014).

Along Profile L2, the Moho gently changes between 110 and 175 km. The synthetic test shows that, for a slightly dipping Moho (e.g., 11.3°), the CCP images represent the input Moho model well. In contrast, along Profiles L3 and L4, the Moho depth changes abruptly with a step of ~10 km (Figures 7c and 7d). The P_ms

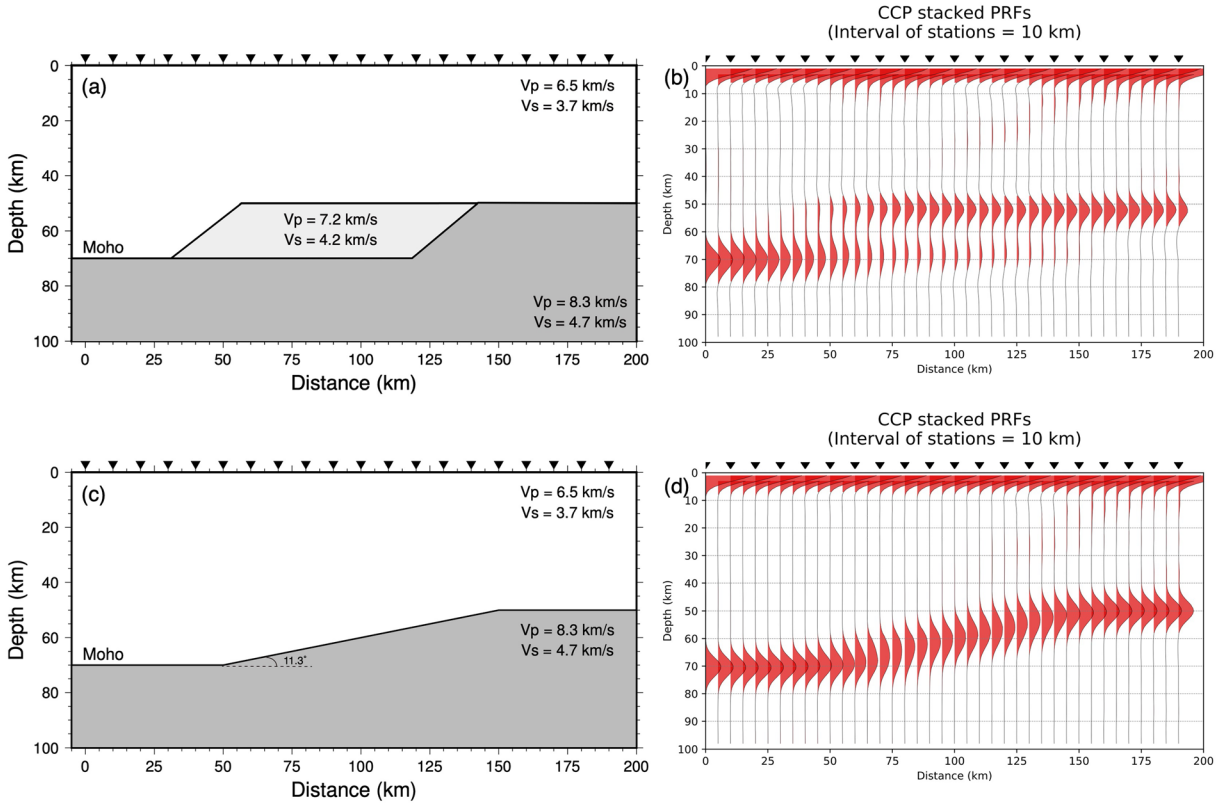

Figure 8. Synthetic PRFs after CCP stacking for two synthetic models with different lateral Moho variations. (a and c) Models with thickened lower crust and gently dipping Moho with dip angle of 11.3°, respectively. Black inverted triangles denote virtual stations. (b and d) CCP stacked PRFs using the model in the left panel.

phases are widened and even show double phases under the peak Moho steps. Previous studies on synthetic PRFs have confirmed that they may be caused by the Moho having large dip angles and that the *Ps-P* differential time and *Ps* amplitudes are affected by the ray parameters (L. Chen et al., 2005; Takedatsu & Olsen, 2016; Yan & Clayton, 2007). On the other hand, sparse station coverage may induce false double P_ms phases (L. Chen et al., 2005). To confirm whether the widened and double P_ms phases in our profiles (Figures 7c and 7d) are produced by a strongly dipping Moho, we constructed an input model with a moderately dipping Moho (21.8°; Figure 9a) and calculated the corresponding PRFs. Wide P_ms phases (Figure 9b) are found in the CCP stacking images for dense stations (station spacing of 10 km), consistent with the widened P_ms phases in Profile L3 (Figure 7c). However, when we reduce the number of stations in the CCP stacking (i.e., set the station spacing to 30 km), double P_ms phases are obtained (Figure 9c). Therefore, we cannot track the real Moho when the stations are widely spaced, but it is confirmed that regardless of the station spacing, the Moho depth changes significantly on a short lateral scale. In any case, the Moho depth changes abruptly across this boundary.

4.2. Crustal Deformations in the SE Tibetan Margin

The Tibetan Plateau has been extruded clockwise along major strike-slip faults toward the southeast (Tapponnier et al., 1982, 2001). Crustal weak zones have been observed by geophysical studies on the SE margin of the Tibetan Plateau (Bai et al., 2010; Bao et al., 2015; Z. Huang et al., 2018; Xie et al., 2017). However, crustal structures are different beneath Tibet and under the Yangtze block. These weak zones are divided into two parts, one in the Songpan-Ganze terrane and the other in the southern Dianzhong sub-block (Figure 10). The lower crust flow model is a reasonable geodynamic interpretation of the uplift of the Tibetan Plateau (Royden et al., 2008). In this model, the plateau is blocked by a stable foreland to the east and produces high-viscosity crustal flow to form steep surface and Moho topography (such as the Sichuan Basin bordered by the Longmenshan fault); the plateau is blocked by a weak foreland to the southeast and

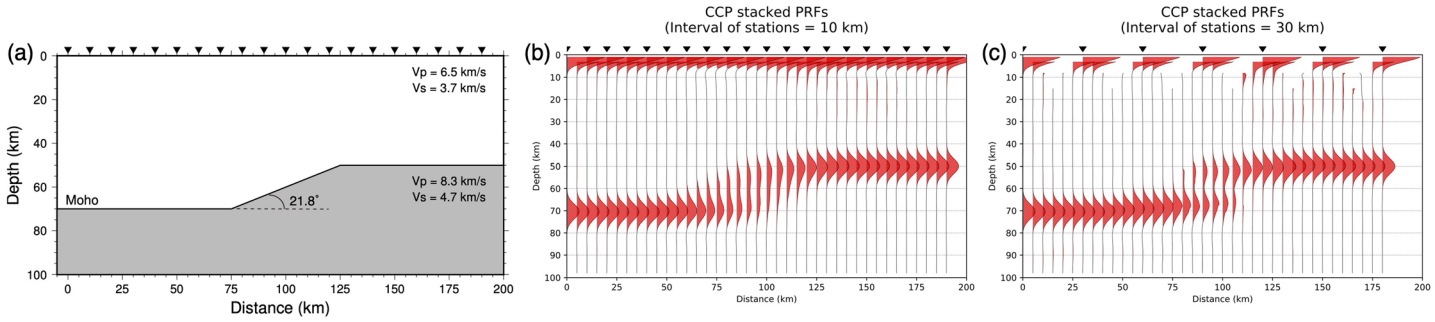

Figure 9. Synthetic PRFs after CCP stacking for a synthetic model with a steeply dipping Moho. (a) The model with a Moho dip angle of 21.8°. (b) CCP stacked PRFs using the model in a with a virtual station interval of 10 km. (c) The same as the middle panel but with a station interval of 30 km.

produces low-viscosity crustal flow to form gentle surface and Moho topography (such as the Dianzhong block with the MT-JQT as the boundary). Our observation of a steeply sloping Moho on the SE plateau margin (under the MT-JQT) is similar to that under the Longmenshan fault. Therefore, the crustal deformation on the SE plateau margin may be explained by the crustal flow model blocked by a stable foreland.

The distinct Moho gradient zone under the MT-JQT across the Tibetan margin has important tectonic implications. The crust of Tibet is thicker than that of the Yangtze Craton (Liu et al., 2014), and there is an abrupt Moho variation across the gradient zone. Relatively high velocity anomalies (Bao et al., 2015; M. Chen

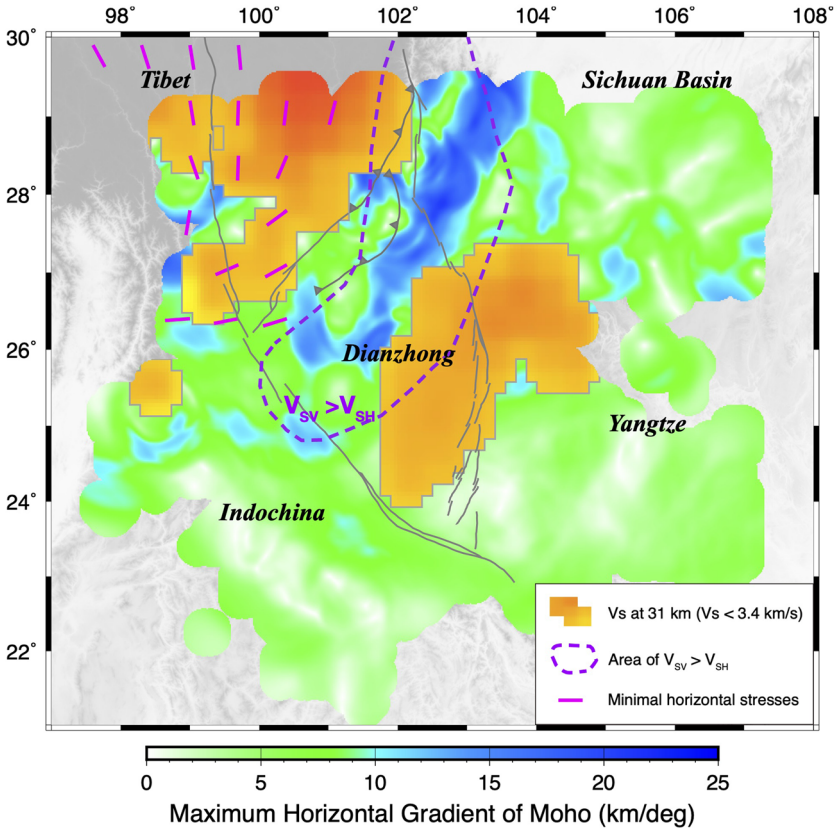

Figure 10. The background colors show the MHGM from model II. Yellow to red colors denote S-wave velocities less than 3.4 km/s at a depth of 31 km (Bao et al., 2015). The dashed purple curve denotes an area with negative radial anisotropy ($V_{SV} > V_{SH}$, i.e., faster vertical velocities) with steeply dipping foliation through the entire crust (Xie et al., 2017). The red bars show the minimal horizontal stresses in the horizontal extension regime (Xu et al., 2016).

et al., 2014; Fu et al., 2017; Z. Huang et al., 2018; Wei et al., 2013; Yao et al., 2008) and negative radial anisotropy ($V_{SH} < V_{SV}$) (Xie et al., 2017) in the lower crust have been detected in the northern region of the Dianzhong subblock (Figure 10), suggesting a rigid deep crust in this region. Thus, the sharp Moho gradient across the Tibetan margin should result from the rheological contrast in the lower crust, that is, weak lower crust beneath Tibet and strong lower crust beneath the foreland of the Yangtze Craton (Dianzhong subblock). Blocked by the rigid foreland, the crustal weak zones are confined to the Songpan-Ganze terrane. The thickening of the Tibetan crust and its southeastward flow mostly occurs along its SE margin (i.e., the crust in front of the Songpan-Ganze terrane is thicker than that in surrounding areas). This interpretation is similar to the crustal thickening across the Longmenshan fault zone on the eastern Tibetan margin (e.g., Qian et al., 2018; Z. Zhang et al., 2009).

The SE plateau margin is currently less active than the eastern plateau margin, with lower strain rates (Pan & Shen, 2017) along the MT-JQT as well as gently varying topography. However, apatite (U-Th)/He and fission track dating results from deeply incised valleys indicate a fast uplift phase that occurred rapidly and was augmented at ~9–13 Ma in the late Miocene (Clark et al., 2005). This uplift corresponds to the rapid southeastward extrusion of the Songpan-Ganze terrane, accommodated by the sinistral strike-slip Xianshuihe fault. Ar-Ar dating of the ductile shear zone along this fault zone constrains the initiation age to ~10 Ma for this left-lateral strike-slip motion (Y. Zhang et al., 2004). The sediments in the Yanyuan Basin, located on the hanging wall of the JQT, were dated by magnetostratigraphy to have initiated at ~3.6 Ma (Lu et al., 2015). Extensional basins developed widely in the Yangtze block of Yunnan Province (Y. Zhang & Li, 2016), suggesting a change in tectonic regime from earlier compression to later extension. This mechanism also explains the local extension in this region to the northwest (Figure 10) (Z. Huang et al., 2018; Z. Xu et al., 2016). We propose that the Moho gradient across the Tibetan margin was mostly established during the late Miocene extrusion-related orogeny. Afterward, gravitational collapse dominated, resulting in local extension and gently varying surface topography across the SE plateau margin. Low correlation coefficients of Moho depths between the $H - \kappa$ stacking and the calculation from the Airy model indicate that crustal gravity in the northern Dianzhong subblock has not been isostatic (W. Wang et al., 2017). The suggestion provides evidence for preservation of a sharp Moho gradient, but the surface topography is smoothed after gravitational collapse.

5. Conclusion

We used the receiver function technique to map the Moho depth under SE Tibet. We used an improved CCP stacking technique to obtain higher-resolution Moho topography and found a sharp Moho gradient zone with lateral heterogeneities on the SE Tibetan margin across the MT-JQT between Tibet and the Yangtze Craton. The Moho gradient zone under the MT-JQT marks the boundary zone between the Songpan-Ganze terrane and the Yangtze block. It was mostly established during the orogeny related to plateau extrusion in the late Miocene that caused thickening of the Tibetan crust. However, the surface has been subsequently smoothed by gravitational collapse in the Pliocene-Quaternary.

Acknowledgments
The seismic data are provided by the China Seismic Array Data Management Center at the Institute of Geophysics, China Earthquake Administration (ChinArray DMC, doi:10.12001/ChinArray.Data, where the cut waveforms around *P* arrivals can be accessed at http://www.chinarraydmc.cn/products/queryData?id=3), and the IRIS Data Management Center. We thank Prof. M. Savage (editor), the Associate Editor, and two anonymous reviewers for their constructive advice. This work was supported by the ChinArray Program (DQJB17A0105) and the National Natural Science Foundation of China (41674044 and 41674049). Most figures were made using GMT (Wessel et al., 2013).

References

Bai, D., Unsworth, M. J., Meju, M. A., Ma, X., Teng, J., Kong, X., et al. (2010). Crustal deformation of the eastern Tibetan plateau revealed by magnetotelluric imaging. *Nature Geoscience*, *3*(5), 358–362. https://doi.org/10.1038/ngeo830

Bao, X., Sun, X., Xu, M., Eaton, D. W. D. W., Song, X., Wang, L., et al. (2015). Two crustal low-velocity channels beneath SE Tibet revealed by joint inversion of Rayleigh wave dispersion and receiver functions. *Earth and Planetary Science Letters*, *415*, 16–24. https://doi.org/10.1016/j.epsl.2015.01.020

Central Energy Resources Team. (2016). *Generalized geology of the far east (geo3al)*. US Geological Survey. https://catalog.data.gov/dataset/generalized-geology-of-the-far-east-geo3al

Chen, L., Wen, L., & Zheng, T. (2005). A wave equation migration method for receiver function imaging: 1. Theory. *Journal of Geophysical Research*, *110*(B11), B11309. https://doi.org/10.1029/2005JB003665

Chen, M., Huang, H., Yao, H., van der Hilst, R., & Niu, F. (2014). Low wave speed zones in the crust beneath SE Tibet revealed by ambient noise adjoint tomography. *Geophysical Research Letters*, *41*(2), 2013GL058476. https://doi.org/10.1002/2013GL058476

Clark, M. K., House, M. A., Royden, L. H., Whipple, K. X., Burchfiel, B. C., Zhang, X., & Tang, W. (2005). Late Cenozoic uplift of southeastern Tibet. *Geology*, *33*(6), 525–528.

Clark, M. K., & Royden, L. H. (2000). Topographic ooze: Building the eastern margin of Tibet by lower crustal flow. *Geology*, *28*(8), 703–706. https://doi.org/10.1130/0091-7613(2000)28<703:TOBTEM>2.0.CO;2

Crotwell, H. P., Owens, T. J., & Ritsema, J. (1999). The TauP toolkit: Flexible seismic travel-time and ray-path utilities. *Seismological Research Letters*, *70*, 154–160. https://doi.org/10.1785/gssrl.70.2.154

Dueker, K. G., & Sheehan, A. F. (1997). Mantle discontinuity structure from midpoint stacks of converted P to S waves across the Yellowstone hotspot track. *Journal of Geophysical Research: Solid Earth*, *102*(B4), 8313–8327. https://doi.org/10.1029/96JB03857

Eagar, K. C., Fouch, M. J., & James, D. E. (2010). Receiver function imaging of upper mantle complexity beneath the Pacific Northwest, United States. *Earth and Planetary Science Letters*, *297*(1–2), 141–153. https://doi.org/10.1016/j.epsl.2010.06.015

England, P., & Houseman, G. (1986). Finite strain calculations of continental deformation: 2. Comparison with the India-Asia collision zone. *Journal of Geophysical Research: Solid Earth*, *91*(B3), 3664–3676.

Frederiksen, A. W., & Bostock, M. G. (2000). Modelling teleseismic waves in dipping anisotropic structures. *Geophysical Journal International*, *141*(2), 401–412. https://doi.org/10.1046/j.1365-246X.2000.00090.x

Fu, Y. V., Gao, Y., Li, A., Li, L., & Chen, A. (2017). Lithospheric structure of the southeastern margin of the Tibetan Plateau from Rayleigh wave tomography. *Journal of Geophysical Research: Solid Earth*, 4631–4644. https://doi.org/10.1002/2016JB013096

Huang, H., Yao, H., & Van Der Hilst, R. D. (2010). Radial anisotropy in the crust of SE Tibet and SW China from ambient noise interferometry. *Geophysical Research Letters*, *37*. https://doi.org/10.1029/2010GL044981

Huang, Z., Wang, L., Xu, M., & Zhao, D. (2018). *P* wave anisotropic tomography of the SE Tibetan Plateau: Evidence for the crustal and upper-mantle deformations. *Journal of Geophysical Research: Solid Earth*, 1–22. https://doi.org/10.1029/2018JB016048

Kennett, B. L. N., & Engdahl, E. R. (1991). Traveltimes for global earthquake location and phase identification. *Geophysical Journal International*, *105*(2), 429–465. https://doi.org/10.1111/j.1365-246X.1991.tb06724.x

Kreemer, C., Blewitt, G., & Klein, E. C. (2014). A geodetic plate motion and global strain rate model. *Geochemistry, Geophysics, Geosystems*, *15*(10), 3849–3889.

Langston, C. A. (1979). Structure under Mount Rainier, Washington, inferred from teleseismic body waves. *Journal of Geophysical Research: Solid Earth*, *84*(B9), 4749–4762. https://doi.org/10.1029/JB084iB09p04749

Ligorría, J. P., & Ammon, C. J. (1999). Iterative deconvolution and receiver-function estimation. *Bulletin of the Seismological Society of America*, *89*(5), 1395–1400. http://www.bssaonline.org/content/89/5/1395.abstract

Liu, Q. Y., van der Hilst, R. D., Li, Y., Yao, H. J., Chen, J. H., Guo, B., et al. (2014). Eastward expansion of the Tibetan Plateau by crustal flow and strain partitioning across faults. *Nature Geoscience*, *7*(5), 361–365. https://doi.org/10.1038/ngeo2130

Lu, H., Wang, E., & Li, S. (2015). Rotational deformation of the southeastern margin of Tibet: A paleomagnetic study of the Yanyuan basin, Sichuan Province (in Chinese with English abstract). *Geology in China*, *42*(5), 1188–1201.

Molnar, P., & Tapponnier, P. (1975). Cenozoic tectonics of Asia: Effects of a continental collision. *Science*, *189*(4201), 419–426. https://doi.org/10.1126/science.189.4201.419

Pan, Y., & Shen, W. B. (2017). Contemporary crustal movement of southeastern Tibet: Constraints from dense GPS measurements. *Scientific Reports*, *7*(1), 1–7. https://doi.org/10.1038/srep45348

Qian, H., Mechie, J., Li, H., Xue, G., Su, H., & Cui, X. (2018). Structure of the crust and mantle down to 700 km depth beneath the Longmenshan from *P* receiver functions. *Tectonics*, *37*(6), 1688–1708. https://doi.org/10.1029/2017TC004726

Royden, L. H., Burchfiel, B. C., & van der Hilst, R. D. (2008). The geological evolution of the Tibetan Plateau. *Science*, *321*(5892), 1054–1058. https://doi.org/10.1126/science.1155371

Shen, Z. K., Lü, J., Wang, M., & Bürgmann, R. (2005). Contemporary crustal deformation around the southeast borderland of the Tibetan Plateau. *Journal of Geophysical Research: Solid Earth*, *110*(11), 1–17. https://doi.org/10.1029/2004JB003421

Sun, Y., Niu, F., Liu, H., Chen, Y., & Liu, J. (2012). Crustal structure and deformation of the SE Tibetan plateau revealed by receiver function data. *Earth and Planetary Science Letters*, *349–350*, 186–197. https://doi.org/10.1016/j.epsl.2012.07.007

Takedatsu, R., & Olsen, K. B. (2016). Estimation of lateral variations of the Mohorovičić discontinuity using 2D modeling of receiver functions. *Bulletin of the Seismological Society of America*, *106*(2), 337–348. https://doi.org/10.1785/0120150126

Tapponnier, P., Peltzer, G., Le Dain, A. Y., Armijo, R., & Cobbold, P. (1982). Propagating extrusion tectonics in Asia: New insights from simple experiments with plasticine. *Geology*, *10*(12), 611–616. https://doi.org/10.1130/0091-7613(1982)10<611:petian>2.0.co;2

Tapponnier, P., Zhiqin, X., Roger, F., Meyer, B., Arnaud, N., Wittlinger, G., & Jingsui, Y. (2001). Oblique stepwise rise and growth of the Tibet plateau. *Science*, *294*(5547), 1671–1677. https://doi.org/10.1126/science.105978

Tromp, J., Komatitsch, D., & Liu, Q. (2008). Spectral-element and adjoint methods in seismology. *Communications in Computational Physics*, *3*(1), 1–32.

Wang, P., Wang, L., Mi, N., Liu, J., Li, H., Yu, D., et al. (2010). Crustal thickness and average Vp/Vs ratio variations in southwest Yunnan, China, from teleseismic receiver functions. *Journal of Geophysical Research: Solid Earth*, *115*(11). https://doi.org/10.1029/2009JB006651

Wang, W., Wu, J., Fang, L., Lai, G., & Cai, Y. (2017). Crustal thickness and Poisson's ratio in southwest China based on data from dense seismic arrays. *Journal of Geophysical Research: Solid Earth*, *122*(9), 7219–7235. https://doi.org/10.1002/2017JB013978

Wang, W., Wu, J., Fang, L., Lai, G., Yang, T., & Cai, Y. (2014). S wave velocity structure in southwest China from surface wave tomography and receiver functions. *Journal of Geophysical Research: Solid Earth*, *119*(2), 1061–1078. https://doi.org/10.1002/2013JB010317

Wei, W., Zhao, D., & Xu, J. (2013). P-wave anisotropic tomography in Southeast Tibet: New insight into the lower crustal flow and seismotectonics. *Physics of the Earth and Planetary Interiors*, *222*, 47–57. https://doi.org/10.1016/j.pepi.2013.07.002

Wessel, P., Smith, W. H. F., Scharroo, R., Luis, J., & Wobbe, F. (2013). Generic mapping tools: Improved version released. *Eos, Transactions American Geophysical Union*, *94*(45), 409–410. https://doi.org/10.1002/2013EO450001

Xie, J., Ritzwoller, M. H., Shen, W., & Wang, W. (2017). Crustal anisotropy across eastern Tibet and surroundings modeled as a depth-dependent tilted hexagonally symmetric medium. *Geophysical Journal International*, *209*(1), 466–491. https://doi.org/10.1093/gji/ggx004

Xu, L., Rondenay, S., & van der Hilst, R. D. (2007). Structure of the crust beneath the southeastern Tibetan Plateau from teleseismic receiver functions. *Physics of the Earth and Planetary Interiors*, *165*(3–4), 176–193. https://doi.org/10.1016/j.pepi.2007.09.002

Xu, M., Huang, H., Huang, Z., Wang, P., Wang, L., Xu, M., et al. (2018). Insight into the subducted Indian slab and origin of the Tengchong volcano in SE Tibet from receiver function analysis. *Earth and Planetary Science Letters*. https://doi.org/10.1016/j.epsl.2017.11.048

Xu, X., Ding, Z., Shi, D., & Li, X. (2013). Receiver function analysis of crustal structure beneath the eastern Tibetan plateau. *Journal of Asian Earth Sciences*, *73*, 121–127. https://doi.org/10.1016/j.jseaes.2013.04.018

Xu, Z., Huang, Z., Wang, L., Xu, M., Ding, Z., Wang, P., et al. (2016). Crustal stress field in Yunnan: Implication for crust-mantle coupling. *Earthquake Science*, *29*(2), 105–115. https://doi.org/10.1007/s11589-016-0146-3

Yan, Z., & Clayton, R. W. (2007). A notch structure on the Moho beneath the Eastern San Gabriel Mountains. *Earth and Planetary Science Letters*, *260*(3–4), 570–581. https://doi.org/10.1016/j.epsl.2007.06.017

Yang, Y., & Liu, M. (2013). The Indo-Asian continental collision: A 3-D viscous model. *Tectonophysics*, *606*, 198–211.

Yao, H., Beghein, C., & van der Hilst, R. D. (2008). Surface wave array tomography in SE Tibet from ambient seismic noise and two-station analysis—II. Crustal and upper-mantle structure. *Geophysical Journal International*, *173*(1), 205–219. https://doi.org/10.1111/j.1365-246X.2007.03696.x

Yao, H., van der Hilst, R. D., & Montagner, J.-P. (2010). Heterogeneity and anisotropy of the lithosphere of SE Tibet from surface wave array tomography. *Journal of Geophysical Research*, *115*(B12), B12307. https://doi.org/10.1029/2009JB007142

Zhang, Y., Chen, W., & Yang, N. (2004). ~(40)Ar/~(39)Ar dating of shear deformation of the Xianshuihe fault zone in west Sichuan and its tectonic significance. *Science in China Series D Earth Sciences-English Edition*, *47*, 794–803.

Zhang, Y., & Li, H. (2016). Late Cenozoic tectonic events in east Tibetan Plateau and extrusion-related orogenic system (in Chinese with English abstract). *Geology in China*, *43*(6), 1829–1852. https://doi.org/10.12029/gc20160601

Zhang, Z., Wang, Y., Chen, Y., Houseman, G. a., Tian, X., Wang, E., & Teng, J. (2009). Crustal structure across Longmenshan fault belt from passive source seismic profiling. *Geophysical Research Letters*, *36*(17), L17310. https://doi.org/10.1029/2009GL039580

Zhao, B., Huang, Y., Zhang, C., Wang, W., Tan, K., & Du, R. (2015). Crustal deformation on the Chinese mainland during 1998–2014 based on GPS data. *Geodesy and Geodynamics*, *6*(1), 7–15.

Zhu, L., & Kanamori, H. (2000). Moho depth variation in southern California from teleseismic receiver functions. *Journal of Geophysical Research*, *105*(B2), 2969. https://doi.org/10.1029/1999jb900322